Journal of Applied Sciences

ISSN 1812-5654

science alert

ANSInet
an open access publisher
http://ansinet.com

Journal of Applied Sciences 11 (10): 1698-1706, 2011
ISSN 1812-5654 / DOI: 10.3923/jas.2011.1698.1706

Flame Development Study at Variable Swirl Level Flows in a Stratified CNG DI Combustion Engine using Image Processing Technique

Yohannes T. Anbese, A. Rashid A. Aziz and Zainal Ambri B.A. Karim
Department of Mechanical Engineering, Universiti Teknologi PETRONAS, Bandar Seri Iskandar, 31750 Tronoh, Perak, Malaysia

Abstract: This study aims to investigate the characteristics of flame development in a lean-stratified combustion of CNG in a single cylinder Direct Injection (DI) engine at a specific motor speed and fixed injection timing and air-fuel ratio by varying only the swirl level at the intake. The engine is set to run at 1800 rpm with half-load throttled. The ignition advance is adjusted at 21.5 BTDC and to create an overall lean and stratified mixture, injection timing is set at 61 BTDC with fuel/air equivalence ratio of 0.425. By positioning the swirl-control-valves just before the two intake valves, medium tumble, medium swirl and high swirl intake flow structures are created in the cylinder and this results variable flow conditions at ignition onset. An endoscope and CCD camera assembly is utilized to capture the flame images from the tumble plane parallel to the cylinder axis every 2 CA degrees after ignition onset for 30 CAs. Using the natural luminosity of the flame and thresholding of the image intensity at certain point the binary image and its boundary vertices are identified. Freeman chain coding and Elliptic Fourier Analysis (EFA) algorithms are utilized to characterize the flame boundary, such as wrinkles and distortions. The result of the study shows that flame growth rate and flame convection velocity are increasing with the swirl level rise. The total combustion duration is thus, shorter in swirl induced combustion than without. However, COV in IMEP which is identified from the cylinder p-v data, is greater in swirl induced flow cases than the tumble flow case. Degree of flame distortion and flame front wrinkles increases with flame size.

Key words: Flame development, swirl flow, tumble flow, spark channel

INTRODUCTION

Flame kernel development period is the time over which the initial flame kernel burns from the spark gap and begins to interact fully with the turbulent flow field. This development stage corresponds to the 0-5% mass fraction burned period (Cho *et al*., 1992; Aleiferis *et al*., 2000, 2004). After the breakdown of the impedance between the spark plug electrodes by the propagation of ionizing streamers from one electrode (cathode) to the other (anode), an electrically conductive path is created between the electrodes. This conductive path is known as spark or plasma channel. The temperature and pressure of this spark channel rises very high, around 60000 k and 20 MPa, respectively as described by Willems and Sierens (2003) and Heywood (1988). This causes a supersonic expansion of the ignition kernel and a strong shock wave propagates outward. Hence, the expansion of the plasma kernel at this stage is governed by the strong shock wave propagation and conduction, rather than combustion. Gradually, the significance of combustion on plasma kernel growth rate increases and the thermo-chemical properties of the fluid near the spark plug become the governing factors of flame kernel development. The combustion reactions at this stage are then sufficiently powerful to lead the expansion of the kernel without supplementary energy supply from the spark plug.

From previous studies it was identified that the quality of a cycle in SI engine can be determined within the short duration of combustion after ignition timing (Aleiferis *et al*., 2000, 2004). Aleiferis *et al*. (2004) showed the benefits of having a high convection velocity in the early flame development time. Other studies of Ting *et al*. (1995) and Xiong *et al*. (2001) portrayed the significance of variable turbulent scale eddies and vortical flows on the flame kernel development. Ting *et al*. (1995) showed the effect of small scale and large scale eddies on the flame growth rate and displacement speed on single cylinder natural gas combustion. The outcome of this study, Ting *et al*. (1995) verified that the flame growth rate is able to correlate best with the level of high frequency, small eddy turbulence. On the other hand

Corresponding Author: Yohannes T. Anbese, Department of Mechanical Engineering, Universiti Teknologi PETRONAS, Bandar Seri Iskandar, 31750 Tronoh, Perak, Malaysia

Xiong *et al*. (2001) showed that vortex strength had a greater influence on kernel flame growth than a vortex size. And also it identifies that vortex enhances flame growth rate significantly, when its interaction with the flame kernel is in the early development period.

The current study investigates the significance of variable swirl levels of air intake on flame development characteristics in a direct injection CNG engine. Air-fuel ratio, injection timing and ignition timing are all set to be constant. The objective is to identify flame growth rate and convection speed and parameters that can influence the flame growth rate, such as flame front wrinkles and distortion, of a developing flame at 1800 rpm and partial load by varying the swirl level of the air intake.

MATERIALS AND METHODS

A single-cylinder Hydra research engine with optical access to the combustion chamber is used for the study. This four-valve engine has a cylinder volume of 399.25 cm^3, 76 mm bore and 88 mm stroke. Both of the intake valve equipped with butterfly type swirl valves for swirl flow generation at the intake. For this study one of the valves was pinned in an open position (0% closed) and the other one was pinned on 0, 50 and 100% closed positions so that medium tumble, medium swirl and high swirl flows are generated in the cylinder, respectively and yield different characteristic turbulent eddies near spark plug. Optical access into the engine cylinder is available through a 10 mm diameter hole for camera endoscope at the intake side with 30 deg installation angles and another similar size hole for laser access with 16 deg installation angles normal to the camera viewing direction. The laser optical access was not utilized for this specific study. Details of the engine data are given in Table 1. The operating conditions for the study were; engine speed 1800 rpm, injection timing set at 61 BTDC, air-fuel-ratio (A/F) 40.5 (λ = 2.35) and ignition timing was set at 21.5 BTDC.

Fuel stratification is created using a stratified combustion piston, as well delaying the injection timing. The in-cylinder pressure was measured with a water cooled piezoelectric pressure transducer connected to KISTLER charge amplifier and digitized by the National Instruments PCI-6034E device. The pressure data is used to determine the mass burn fraction in the combustion chamber, IMEP and COV in IMEP. Flame images are taken by a HiSence 12 bit CCD camera with image intensifier unit Hamamatsu CA2098. The camera endoscope which is of type AVL KARL STORZ # M00060 30° is inserted into the engine cylinder and steered to have a view field parallel to the cylinder axis which is of the tumble plane. Filtered air at 6 bars is supplied to the endoscope cooling channel for the purpose of cooling.

Table 1: Engine specification

Data	Values
Displacement volume	399.25 cm^3
Cylinder bore	76 mm
Cylinder stroke	88 mm
Compression ratio	14
Exhaust valve open	10 ATDC
Exhaust valve closed	45 BBDC
Intake valve open	12 BTDC
Intake valve closed	48 ABDC

Calibration of the pixel size and camera focus adjustment are done outside the engine cylinder by taking into consideration the distance between the endoscope window tip and the spark electrodes center and keeping the 30° endoscope installation angle. The calibration took into account the image deformations due to the endoscopic imaging and identified that one pixel is equivalent to 0.092 mm within 12.5 mm radius from the center of the endoscope view, whereas, it is equivalent to 0.126 mm out side of this radius of view.

Flame images are collected every 2°CA difference starting from 20 BTDC for 30 CA degrees. To obtain quantitative information from the flame images, a computer algorithm is prepared on Matlab to calculate the projected enflamed area, the perimeter and centroid of the flame area. This flame physical information can be used to identify flame growth rate, flame center displacement and flame distortion as illustrated in Fig. 1.

Flame images taken from the combustion cylinder are very likely accompanied with back ground noises due to light reflecting surfaces and others. Therefore, image filtering will be considered as a pre-processing step. The Gaussian filtering technique is applied for filtering the high frequency noises with the 2D Gaussian kernel given in Eq. 1. Image enhancement also considered by stretching the dynamic range of the flame image histogram as discussed by Kabir *et al*. (2007):

$$G(x,y) = \frac{1}{2\pi\sigma^2} e^{-\frac{x^2+y^2}{2\sigma^2}} \quad (1)$$

After filtering out the noises from the raw flame images, the binary image and its boundary are identified by intensity thresholding based on the statistical values of the gray levels of the flame images. For this purpose, let the pixels of the image be represented by L gray levels. The number of pixels in level i is denoted by hi and the total number of pixels is denoted by N. The gray level histogram is normalized and regarded as probability distribution function:

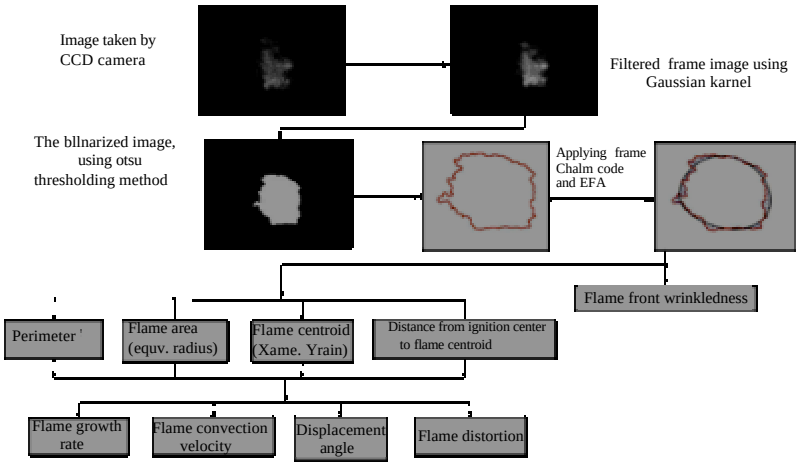

Fig. 1: Flame image processing algorithm

$$P_i = \frac{h_i}{N}, \qquad P_i \geq 0, \qquad \sum_{i=1}^{L} P_i = 1 \tag{2}$$

Suppose the pixels are divided into two classes C_0 and C_1 by a threshold value at k. C_0 denotes pixels with levels [0, 1, …, k] and C_1 denotes pixels with levels [k+1, …, L-1].

The probabilities of class occurrences ω, class mean levels μ and class variance for both classes are given by:

$$\omega_0 = \sum_{i=0}^{k} p_i, \qquad \omega_1 = \sum_{i=k+1}^{L-1} P_i = 1 - \omega_0 \tag{3}$$

$$\mu_0 = \sum_{i=0}^{k} \frac{iP_i}{\omega_0}, \qquad \mu_1 = \sum_{i=k+1}^{L-1} \frac{iP_i}{\omega_1} = \frac{\mu_T - \mu_k}{1 - \omega_0} \tag{4}$$

$$\sigma_0^2 = \sum_{i=0}^{k} (i-\mu_0)^2 P_i, \quad \sigma_1^2 = \sum_{i=k+1}^{L-1} (i-\mu_1)^2 P_i = \sigma_T^2 - \sigma_0^2 \tag{5}$$

where, μ_T, μ_k and σ_T^2 are given by:

$$\mu_T = \sum_{i=0}^{L-1} iP_i, \quad \sigma_T^2 = \sum_{i=0}^{L-1} (i-\mu_T)^2 P_i, \quad \mu_k = \sum_{i=0}^{k} iP_i \tag{6}$$

Otsu (1979) suggested minimizing the weighted sum of within-class variances of the object and background pixels to establish an optimum threshold, in other word, maximization of between-class variance. The between-class variance, σ_B^2, can be identified by:

$$\sigma_B^2 = \omega_0 (\mu_0 - \mu_T)^2 + \omega_1 (\mu_1 - \mu_T)^2 \tag{7}$$

Hence, the optimal threshold is the one that maximizes σ_B^2. With this threshold value the binary image will be identified and the outer contour of the binary image is, then, taken as the flame boundary which is expressed as N by 2 vertices. Freeman chain-code and Elliptic Fourier Analysis (EFA) techniques are utilized to characterize the flame boundaries. First, the motion along the boundary is coded with the 8-direction Freeman chain code, as shown on Fig. 2. Using the outputs of the chain code a truncated Fourier series expansion of the closed contour of the flame projected on the X and Y-axis is identified using Eq. 8 and 9 as illustrated by Trier *et al.* (1996):

$$X_N(t) = A_0 + \sum_{n=1}^{N} a_n \cos\left(\frac{2n\pi t}{T}\right) + b_n \sin\left(\frac{2n\pi t}{T}\right) \tag{8}$$

$$X_N(t) = C_0 + \sum_{n=1}^{N} c_n \cos\left(\frac{2n\pi t}{T}\right) + d_n \sin\left(\frac{2n\pi t}{T}\right) \tag{9}$$

where, t is the step required to traverse one pixel along the closed contour, $t_{p-1} < t < t_p$ for 1 = p = k and k is the total number of codes describing the boundary contour. n is the number of Fourier harmonics required to generate the approximate flame boundary. T is the basic period of the chain-code, $T = t_k$. A_0 and C_0 are the bias coefficients. N is the total number of Fourier harmonics needed to generate an accurate approximation of the flame boundary.

Each EF harmonic has four coefficients. The nth set of these coefficients is defined as:

Δx	Δy	8-code
1	0	0
1	1	1
0	1	2
-1	1	3
-1	0	4
-1	-1	5
0	-1	6
1	-1	7

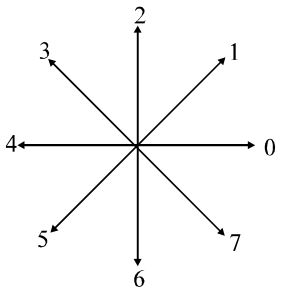

Fig. 2: The 8-direction Freeman chain code schematic

$$a_n = \frac{T}{2n^2\pi^2}\sum_{p=1}^{k}\frac{\Delta x_p}{\Delta t_p}\left[\cos\left(\frac{2n\pi t_p}{T}\right)-\cos\left(\frac{2n\pi t_{p-1}}{T}\right)\right] \quad (10)$$

$$b_n = \frac{T}{2n^2\pi^2}\sum_{p=1}^{k}\frac{\Delta x_p}{\Delta t_p}\left[\sin\left(\frac{2n\pi t_p}{T}\right)-\sin\left(\frac{2n\pi t_{p-1}}{T}\right)\right] \quad (11)$$

$$c_n = \frac{T}{2n^2\pi^2}\sum_{p=1}^{k}\frac{\Delta y_p}{\Delta t_p}\left[\cos\left(\frac{2n\pi t_p}{T}\right)-\cos\left(\frac{2n\pi t_{p-1}}{T}\right)\right] \quad (12)$$

$$d_n = \frac{T}{2n^2\pi^2}\sum_{p=1}^{k}\frac{\Delta y_p}{\Delta t_p}\left[\sin\left(\frac{2n\pi t_p}{T}\right)-\sin\left(\frac{2n\pi t_{p-1}}{T}\right)\right] \quad (13)$$

where, Δx_p and Δy_p are the spatial changes in the x and y projections of the chain code, respectively, at link p. $\Delta t_p = \sqrt{\Delta x_p^2 + \Delta y_p^2}$ is the step change required to traverse link p of the chain code:

$$t_p = \sum_{i=1}^{p}\Delta t_i$$

is the number of steps required to traverse the first p components or links of the chain code.

Shape descriptions need to be invariant with rotation, size, translation and starting point on the contour, to use them in any size of flame image. To obtain features that are independent of a specific starting point, it is necessary to identify the angle between the starting point and the first semi-major axis, using the first set of harmonic coefficients:

$$\theta_1 = \frac{1}{2}\arctan\left[\frac{2(a_1b_1 + c_1d_1)}{a_1^2 - b_1^2 + c_1^2 - d_1^2}\right] \quad 0 \le \theta_1 \le 2\pi \quad (14)$$

Then, the coefficients can be rotated to achieve a zero phase shift:

$$\begin{bmatrix} a_n^* & c_n^* \\ b_n^* & d_n^* \end{bmatrix} = \begin{bmatrix} \cos\theta_1 & \sin\theta_1 \\ -\sin\theta_1 & \cos\theta_1 \end{bmatrix}\begin{bmatrix} a_n & c_n \\ b_n & d_n \end{bmatrix} \quad (15)$$

Next, the rotation invariant descriptors can be identified by rotating the semi-major axis of the first harmonic by angle ψ_1 until it was parallel to the positive x-axis of the first quadrant:

$$\psi_1 = \arctan\left[\frac{y_1^*(0)}{x_1^*(0)}\right] = \arctan\left(\frac{c_1^*}{a_1^*}\right) \quad (16)$$

where, $y_1^*(0)$ and $x_1^*(0)$ were found by applying Eq. 15 into Eq. 8 and 9.

To obtain size invariant descriptors, the coefficients should be divided by the magnitude of the semi-major axis, E^*, of the first ellipse:

$$E^* = \sqrt{a_1^{*2} + c_1^{*2}} \quad (17)$$

Setting the bias terms A_0 and C_0 to zero made the EF coefficients to be invariant to translation

RESULTS AND DISCUSSION

Variable turbulent intensity flows are generated by closing the swirl control valve at different levels ahead of the intake valves so that the flow would have a higher velocity than it had in the absence of swirl. The use of swirl valve control for turbulence generation could increase the pressure drop and reduces the volumetric efficiency. Consequently, IMEP dropped with the increase of swirl level as shown in Table 2. The reduction in IMEP was 1 and 8.5% for medium and high swirl flows, respectively. Heywood (1988) indicated that there might be a power penalty due to the use of significant swirl at induction which can reach up to 10% with full-open swirl control valve (no swirl case), the engine operates with a medium tumble flow. Tumble flows in an engine cylinder have high rate of turbulence generation than swirl flows. In a tumble induction case, bulk flow decaying will start early in the compression stroke. This can create small scale-eddy dominated flow near end of compression. Ting *et al.* (1995) showed that small scale eddies have significant effect on flame-front wrinkling and fuel burning rate enhancement than the large scale turbulent eddies. Besides, cyclic variation will be less when burning is in small scale dominated turbulent flow due to homogeneity. Therefore, fuel burning rate at the early flame development can be faster in a tumble flow case (no swirl) than the two swirl induction cases. However, since small scale turbulence has a faster rate of decay than the large scale eddies, the turbulence intensity will decline faster during fuel burning in the tumble flow case and hence the overall combustion period becomes longer than the swirl flow cases.

Whereas, in the swirl intake flow case, due to the conducive nature of the combustion cylinder design for the swirling flow, decaying of bulk flow into turbulent flow starts late in the compression stroke. This can create a flow that retains its bulk flow kinetic energy past TDC and the flow near TDC might be dominated by large scale turbulence. As this large scale eddies are sources for small scale eddies, turbulence generation will continue during combustion and increase burning rate. This is the reason why the overall burning time in swirl induction case was almost half of the tumble flow case, as shown in Table 2. However, the swirl flow case may have high cycle-to-cycle combustion variation due to the high proportion of large scale flows in the early flame development period (Heywood, 1988; Ting *et al*., 1995). The high cyclic variability is due to the random motion of the large scale eddies and their convection of the small flame ball in a random direction. As the flame ball gets larger in size, all scales of turbulent eddies enhance the expansion and the burning rate of the flame.

The fuel burn fraction is plotted against CA for the three flow conditions, as shown in Fig. 3. The RassWeiler model is used to identify the mass fraction burn of CNG and positive value of fuel fraction burn is observed after TDC. Effects of turbulent eddies can be observed on the fuel burn fraction curves of Fig. 3. As discussed before, due to the small-scale dominated flow of the medium tumble intake case before TDC, the rate of fuel burn is high in the early flame development period. A similar rate of burning was observed on the medium swirl level flow which is expected to have mixed characteristics of tumble and swirl flows as discussed by Zhao *et al*. (2002). After 8 ATDC (when 35% of the fuel burned) the fuel burn rate of the medium tumble slowed down, whereas the medium swirl continued with the same pace till 80% of the fuel burned. On the other hand, rate of burning for the high swirl flow case started with a slower rate than the other two cases and then becomes faster after 7.5 ATDC. That was because the availability of large scale eddies and the well conserved bulk kinetic energy past TDC in both swirl intake cases become sources for further turbulence generations.

According to the COV_{IMEP} value shown in Table 2, the cyclic variation is high with increased swirl level. There might be some discrepancies on using the average cylinder pressure for identifying fuel burn rate, especially on the high swirl induction case where combustion instability is high (13.85% COV_{IMEP}). However, the mass burn curve trends show that burning rate is much faster with swirl induction than with out. This gives us short combustion duration in swirl induced flow than with a flow without swirl. Ninety percent of the fuel is burned in

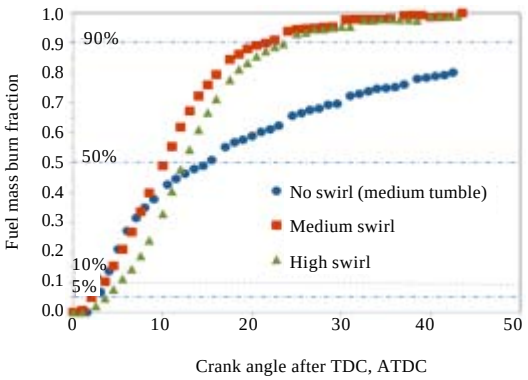

Fig. 3: Mass fuel burn fraction for the different swirl flow condition

Table 2: Engine performance parameter

Intake condition	IMEP (bar)	COV in IMEP (%)	%drop in IMEP (%)	5% fuel burn time (msec)	90% fuel burn time (msec)
Medium tumble	3.89	4.40	-	2.27	7.52
Medium swirl	3.85	9.40	1.0	2.18	3.98
High swirl	3.56	13.85	8.5	2.36	4.07

3.98 and 4.07 msec in the case of medium and high swirl flow conditions, respectively. But in medium tumble case it takes, 7.52 msec, nearly twice the time taken in swirl flow cases. These show that combustion becomes faster by increasing swirl level of intake air; even though, there is cyclic variability and high probability of misfires. Zhao *et al*. (2002) indicated that under lean condition an excessive turbulent level might not be desired.

Figure 4 shows the variations of equivalent radius of mean flame with time. It can be observed that for all flow cases the equivalent flame radius grows more than 2 mm radius within 0.15 msec After Ignition Timing (AIT). This high rate of growth is achieved due to expansion of the extremely high temperature and pressure ignition kernel by a strong shock wave as discussed in Heywood (1988). After that, the ignition kernel cools down and shrinks to a smaller size of about 1.5 mm at 3 msec AIT. This flame size is the minimum size recorded in all flow cases and this period can be taken as ignition kernel development period. In this period flame growth is not a function of turbulent flow characteristics. It is the function of the ignition system. At the end of the ignition kernel formation process, Zhao *et al*. (1994) found flame size to be 1 mm. Starting from 3 msec after ignition onset, the effect of fuel combustion on flame growth becomes apparent and the flame growth rate curve for the different swirl level intake follows different trend depending on the turbulent flow field characteristics surrounding the flame kernel.

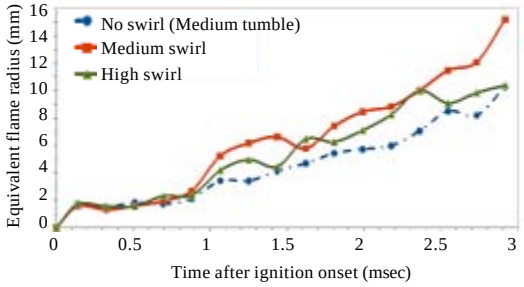

Fig. 4: Equivalent flame radiuses at different crank angle after ignition for variable swirl level intakes

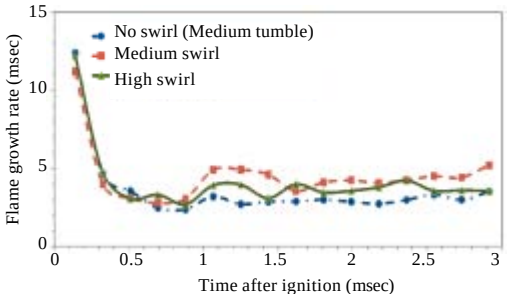

Fig. 5: Flame growth rate after ignition timing for variable swirl level intakes

It is observed that the medium and high swirl flow cases gain more increase in flame size than the tumble flow case. However, the increase in equivalent radius of the flame is not uniform and the non uniformity of the curves is increasing with swirl level rise. The high-frequency small scale eddies in the tumble induction seem to yield a uniform flame growth than the large scale dominated flow of the other two swirl induction cases, as shown in Fig. 4.

Flame growth rate is plotted against time as shown on Fig. 5. It is taken to be the rate of change of mean flame equivalent radius. It can be observed from the figure that the growth rate for the three flow cases starts at a very high value and drops sharply till it attains the minimum rate. Then it shows a short rise and after a certain time it attains a constant rate of growth. A similar trend is recorded by Willems and Sierens (2003). The initial gain of a very high rate of growth is due to the expansion by strong shock wave of the plasma kernel as discussed earlier. The flame growth rate in the development period is high for swirl induction cases and lower for medium tumble intake case, despite the high burning rate of the later in the early flame development period (Fig. 3, 5). This is probably due to quenching of the flame kernel in the tumble induction case in contact with cool surfaces such as spark plug electrodes which is to be discussed later.

Flame convection is another important parameter that can influence combustion performance. Flame convection magnitude and direction can be affected by the bulk flow velocity and the motion of large scale eddies that have random motion (Josefsson *et al*., 2001; Ting *et al*., 1995). When the flame kernel is smaller than the average eddy size, the small flame ball will be randomly convected by the flow due to the random motion of the eddies. Besides, as the size of the flame increases and the piston reaches TDC the squish flow and the bowl on piston crown will have significant influence on flame convection direction (Ghasemi and Djavareshkian, 2010).

Figure 6-9 are plotted to convey flame convection and flame center displacement phenomenon. The random displacement of flame centroid at various times is plotted against crank angle on Fig. 6. It depicts that in the early period of development, the flame starts to grow and expand on the left side of the ignition point for all the three flow cases. Then the flame is displaced to the right of the ignition point in later time for all flow cases. However, time of displacement to the right of spark center for each cases are different. In the case of both swirl flow intakes, the flame moves to the right early before TDC, starting from 8 BTDC (1.25 msec AIT), as shown in Fig. 6b and c. Whereas for the medium tumble case the flame moves to the right after 2 ATDC (2.18 msec AIT) (Fig. 6a). The eccentric bowl on the piston crown, shown in Fig. 7 and the squish flow generated near TDC which is able to intensify the swirl flow as discussed by Zhao *et al*. (2002), favor the displacement of the flame towards the right of the ignition point in the early development period of the two swirl induction cases.

As it is observed from Fig. 8 and 9, the farness of the flame kernel from the spark center literally shows significant influence on flame growth rate. Based on the flame image analysis within 30CA (3 msec) after ignition onset, the average flame position in medium tumble, medium swirl and high swirl flow cases is 3.14 mm at 94.67°, 9.78 mm at 84.27° and 5.11 mm at 74.91° away from the spark center, respectively. Their respective mean flame growth rate within this period of time is 3.38, 4.57 and 3.92 msec. The flame kernel which is far from the spark plug might avoid flame surface quenching, hence get better growth rate than the one which is very near to spark electrodes. The convection of the flame kernel away from the spark center, on the other side, is a function of flow characteristics around the spark plug. As it's observed from the discussed results, the turbulent flow in the medium swirl flow case convects flame kernel far away from the spark center relative to the other two flow

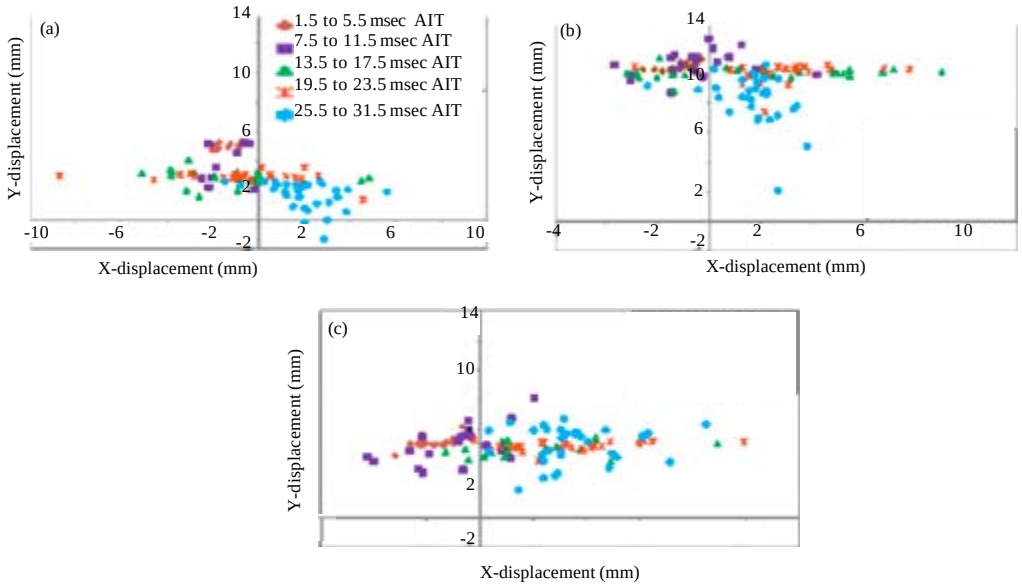

Fig. 6: Flame center displacement from the center of the spark plug electrode gap at different time AIT in (a) medium tumble (no swirl) flow, (b) medium swirl flow and (c) high swirl flow cases

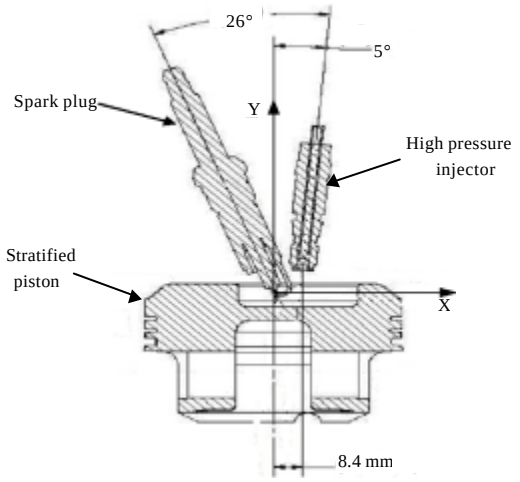

Fig. 7: Schematic diagram of piston, spark plug and injector arrangement with off-center bowl

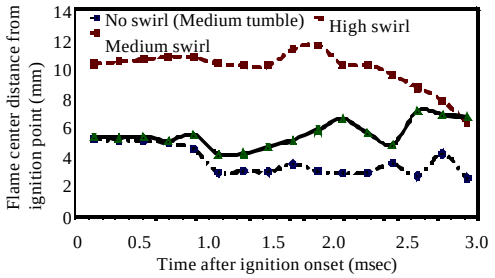

Fig. 8: Cycle average flame centroid distance from ignition center

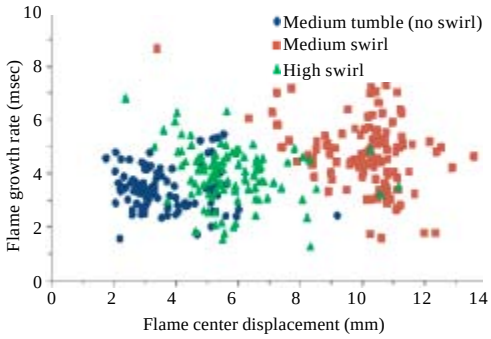

Fig. 9: Relation between flame center displacement and flame growth rate

cases. As a result, a higher flame growth rate is recorded in the medium swirl flow case than the other two cases (Fig. 5, 8).

The measure of flame distortion for the three flow cases is plotted against time as shown on Fig. 10. It is calculated by the ratio of flame perimeter to perimeter of a circle whose radius is equal to the equivalent radius of the flame. It can be noticed that the flame distortion generally follows a similar trend for all flow cases and there is no flame increases in size and starts to interact with the flame distortion up to 0.5 msec AIT. Thereafter, the

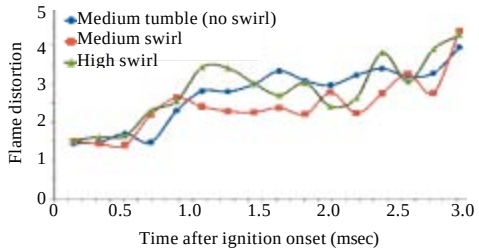

Fig. 10: Flame distortions at different crank angle after ignition onset

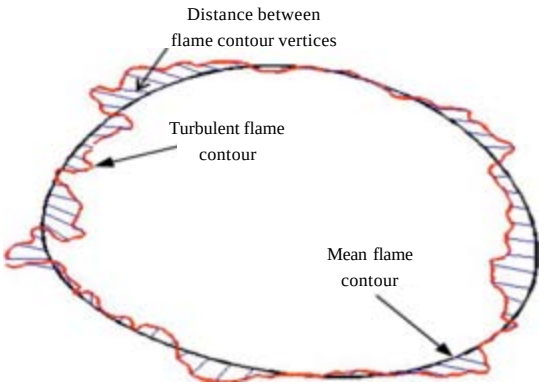

Fig. 11: Schematics of distances between flame contour's vertices

surrounding turbulence. With the size increase flame distortion can be exhibited due to some reasons, such as combustion irregularity caused by local air-fuel variability, flame surface quenching in contact with cool surfaces such as spark plug electrodes and flame stretch by large scale eddies. However, general observation on Fig. 10 shows that the least distorted flame has the better growth rate (in this case medium swirl flow type). The flame distortion is moderately correlated with the flame growth rate.

Flame front wrinkles are approximated from the irregularity of the boundary of the flame. This boundary irregularity can be found from the standard deviation of the distances measured between the vertices of the mean flame contour and the turbulent flame contour. The second harmonics of the elliptic Fourier approximation for the flame boundary yields the mean flame contour, as shown in Fig. 11. The standard deviation of these distances, thus, used to measure degree of flame front wrinkledness. Standard deviation of boundary point distances for the three different cases of swirl levels are plotted against flame equivalent radius as shown in

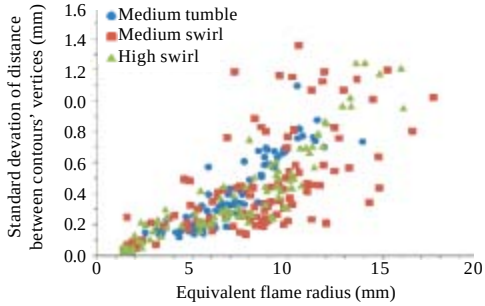

Fig. 12: Standard deviation of distances measured between vertices of turbulent and mean flame contours at variable swirl induction

Fig. 12. It can be observed that in general speaking the flame wrinkles have direct relation with size increase throughout the flame development period. However, the correlation of the wrinkles measure with flame size rise is weaker for medium swirl level case than the other two cases.

CONCLUSION

In this study flame development characteristics are investigated by varying the Swirl Control Valve (SCV) position just before the two intake valves. The following conclusions can be derived from the study.

From the nature of swirl and tumble flow in engine cylinders and from the effect of the generated turbulent eddies, it is possible to conclude that medium swirl flow case showed the best characteristics of the two types of flow to have a high fuel burning and flame expansion rate. Flame displacement away from the spark center, especially in the early period of combustion, is higher in medium swirl flow case than the two other flow cases. This helps to reduce flame quenching by spark plug electrodes when the flame ball is very small in early period. However, the reason why the medium swirl flow case has high flame convection than the high swirl flow case is not clear. The large scale eddies, mean bulk flow and the generated squish near TDC might have their own influence on flame convection, particularly in the early flame development stage. This situation is expected to be clear in the next part of the study when the flow field near spark plug and surrounding the flame is dealt using PIV technique.

Turbulence decaying in tumble flow starts early in compression stroke due to its bulk flow structure and as a result charge flows near TDC will be dominated by small scale eddies that can ultimately increase fuel burning rate. This is the reason to get a fast fuel burning rate in the early combustion time of the medium tumble case than the

two swirl flow cases. However, as a result of its nearness to the spark plug, flame growth rate is lower than the swirl flow cases probably due to quenching by the cool surfaces of the electrodes.

Though turbulence generation is late in swirl flow cases, kinetic energy is conserved well past TDC to generate turbulent eddies which increased burning rate and as a result yields lower overall combustion time than the no swirl case (medium tumble).

Even though the two swirl flow cases enhanced the fuel burning rate and reduce the overall combustion time, the cyclic variability is increased and keeps on increasing with swirl level rise.

Flame front wrinkledness and flame distortion show direct effect on flame growth rate.

The variable level of swirl intake can have different air-fuel mixing rate and as a result, the local air-fuel ratio might be variable at the time of ignition. This can result a variable flame growth rate among the different swirl level intakes in the early flame development period.

REFERENCES

Aleiferis, P.G., A.M.K.P. Taylor, J.H. Whitelaw. K. Ishii and Y. Urata, 2000. Cyclic variations of initial flame kernel growth in a honda VTEC-E lean-burn spark-ignition engine. SAE Trans., 109: 1340-1380.

Aleiferis, P.G., A.M.K.P. Taylor, K. Ishii and Y. Urata, 2004. The nature of early flame development in a lean-burn stratified-charge spark-ignition engine. Combustion Flame, 136: 283-302.

Cho, Y.S., D.A. Santavicca and R.M. Sonntag, 1992. The Effect of Spark Power on Spark Ignited Flame Kernel Growth. SAE International, Warrendale, Pennsylvania, USA.

Ghasemi, A. and M.H. Djavareshkian, 2010. Investigation of the effects of natural gas equivalence ratio and piston bowl flow field on combustion and pollutant formation of a DI dual fuel engine. J. Applied Sci., 10: 1369-1379.

Heywood, J.B., 1988. Internal Combustion Engine Fundamentals. McGraw-Hill Book Company, New York.

Josefsson, G., J. Fischer and I. Magnusson, 2001. Length scale measurements in an engine using PIV and comparison with LDV. Proceedings of 5th International Symposium on Diagnostics and Modeling of Combustion in IC Engines, July 1-4, Nagoya, Japan, pp: 653-660.

Kabir, M.H., M. Abdullah-Al-Wadud, M.A.U. Khan, A. Rashid and S. Ahmad, 2007. Block overlapped intensity-pair distribution approach for image contrast enhancement. Inform. Technol. J., 6: 897-902.

Otsu, N., 1979. A threshold selection method from gray level histogram. IEEE Trans. Syst. Man Cybernetics, 9: 62-66.

Ting, D.S., M.D. Checkel and B. Johansson, 1995. The Importance of High-Frequency, Small-Eddy Turbulence in Spark Ignited, Premixed Engine Combustion. SAE International, Warrendale, Pennsylvania, USA.

Trier, O.D., A.K. Jain and T. Taxt, 1996. Feature extraction methods for character recognition-a survey. Patt. Recog., 29: 641-662.

Willems, H. and R. Sierens, 2003. Modeling the initial growth of the plasma and flame kernel in S.I. engines. J. Eng. Gas Turbines Power, 125: 479-484.

Xiong, Y., W.L. Roberts, M.C. Drake and T.D. Fansler, 2001. Investigation of pre-mixed flame-kernel/vortex interactions via high-speed imaging. Combustion Flame, 126: 1827-1844.

Zhao, F., D.L. Harrington and M.C.D. Lai, 2002. Automotive Gasoline Direct-Injection Engines. SAE International, Warrendale, Pennsylvania, USA.

Zhao, X., R.D. Matthews and J.L. Ellzey, 1994. Numerical simulations of combustion in SI engines: Comparison of the fractal flame model to the coherent flame model. Proceedings of 3rd International Symposium on Diagnostics and Modeling of Combustion in IC Engines, July 11-14, Yokohama, Japan, pp: 157-162.